



Bayesian Evidence for a Nonlinear Damping Model for Coronal Loop Oscillations

Iñigo Arregui^{1,2} ¹ Instituto de Astrofísica de Canarias, Vía Láctea S/N, E-38205 La Laguna, Tenerife, Spain; iarregui@iac.es² Departamento de Astrofísica, Universidad de La Laguna, E-38206 La Laguna, Tenerife, Spain

Received 2021 April 23; revised 2021 June 16; accepted 2021 June 22; published 2021 July 6

Abstract

Recent observational and theoretical studies indicate that the damping of solar coronal loop oscillations depends on the oscillation amplitude. We consider two mechanisms: linear resonant absorption and a nonlinear damping model. We confront theoretical predictions from these models with observed data in the plane of observables defined by the damping ratio and the oscillation amplitude. The structure of the Bayesian evidence in this plane displays a clear separation between the regions where each model is more plausible relative to the other. There is qualitative agreement between the regions of high marginal likelihood and Bayes factor for the nonlinear damping model and the arrangement of observed data. A quantitative application to 101 loop oscillation cases observed with Solar Dynamics Observatory/Atmospheric Imaging Assembly (SDO/AIA) results in the marginal likelihood for the nonlinear model being larger in the majority of them. The cases with conclusive evidence for the nonlinear damping model outnumber considerably those in favor of linear resonant absorption.

Unified Astronomy Thesaurus concepts: [Magnetohydrodynamics \(1964\)](#); [Solar coronal loops \(1485\)](#); [Solar coronal seismology \(1994\)](#); [Bayesian statistics \(1900\)](#); [Bayes factor \(1919\)](#)

1. Motivation

Damped transverse oscillations of solar coronal loops have been the subject of intense observational and theoretical research in the past two decades since their discovery using the Transition Region and Coronal Explorer by Aschwanden et al. (1999) and Nakariakov et al. (1999). Further observations with instrumentation on-board the Solar Dynamics Observatory (SDO) and the Solar TERrestrial RELations Observatory produced an increase in the amount and quality of the data. This has led to the creation of catalogs containing oscillation properties for a large number of events (Goddard et al. 2016; Nechaeva et al. 2019). The analysis of these events shows an empirical relationship between the measured damping ratio and the oscillation amplitude (Goddard & Nakariakov 2016).

The observed damping has been widely attributed to the mechanism of resonant absorption (Goossens et al. 2002; Ruderman & Roberts 2002). The numerical experiments by Magyar & Van Doorselaere (2016) show that for small oscillation amplitudes linear resonant absorption provides a good approximation to the damping properties. For larger amplitudes the nonlinear evolution results in a significantly faster damping than predicted by linear theory. Recent analytical developments by Van Doorselaere et al. (2021), using a mathematical description in terms of Elsässer variables, show that the nonlinear damping time of impulsively excited standing kink modes in coronal loops is inversely proportional to the oscillation amplitude.

Assessing the damping mechanism(s) operating in coronal loop oscillations is crucial to advance in coronal seismology and wave heating investigations. In this study, we confront the theoretical predictions from linear resonant damping and from the nonlinear damping model by Van Doorselaere et al. (2021) with observed loop oscillation properties in the catalog compiled by Nechaeva et al. (2019). The aim is to quantify the evidence for the nonlinear damping model relative to the evidence for resonant absorption in explaining the damping of coronal loop oscillations.

2. Damping Models

The damping of coronal loop oscillations has been widely interpreted in terms of resonant absorption (RA) of standing kink waves in radially inhomogeneous flux tube models (see, e.g., Goossens et al. 2006, 2011). The mechanism is based on the transfer of wave energy from large to small spatial scales in the radial direction. Under the thin tube and thin boundary approximations, the ratio of the damping time τ_d to the oscillation period P is given by the analytical expression (Ruderman & Roberts 2002; Goossens et al. 2002)

$$\frac{\tau_d}{P} \Big|_{M_{\text{RA}}} = \mathcal{F} \frac{\zeta + 1}{\zeta - 1} \frac{R}{l}, \quad (1)$$

with $\zeta = \rho_i/\rho_e$ the ratio of internal to external density, l/R the length of the non-uniform layer at the boundary of the waveguide with radius R , and $\mathcal{F} = 2/\pi$ for a sinusoidal variation of density over the non-uniform layer. The predictions from the damping model M_{RA} given by Equation (1) for the observable damping ratio are determined by the parameter vector $\theta_{\text{RA}} = \{\zeta, l/R\}$.

A recent analytical investigation by Van Doorselaere et al. (2021) has shown that the nonlinear (NL) damping time of standing kink waves is inversely proportional to the oscillation amplitude. The nonlinear evolution of the dynamics produces an energy transfer to small scales in the radial and azimuthal directions. Using a formalism based on the use of Elsässer variables, Van Doorselaere et al. (2021) derive an analytical expression for the damping ratio in the inertial regime of the turbulent cascade given by

$$\frac{\tau_d}{P} \Big|_{M_{\text{NL}}} = 20\sqrt{\pi} \frac{1}{2\pi a} \frac{1 + \zeta}{\sqrt{\zeta^2 - 2\zeta + 97}}, \quad (2)$$

with $a = \eta/R$ the ratio of the displacement η to the loop radius. The predictions from the damping model M_{NL} given by Equation (2) for the observable damping ratio, for known oscillation amplitude, are determined by the parameter vector $\theta_{\text{NL}} = \{R, \zeta\}$.

3. Analysis and Results

Our judgment on the evidence in favor of any of the two models with respect to the other in explaining a set of observations is based on the use of Bayesian reasoning (see, e.g., Jaynes 2003; Gregory 2005; Lindley 2014). The philosophy and methodology of this approach and early applications to solar coronal seismology are discussed in Arregui (2018).

As first noticed by Goddard & Nakariakov (2016), when the damping ratio for a large number of loop oscillation events is plotted against their oscillation amplitude, the data are scattered forming a cloud with a triangular shape. Larger amplitudes correspond in general to smaller damping ratio values and vice versa (see Figure 2 in Goddard & Nakariakov 2016 or Figure 6 (bottom right) in Nechaeva et al. 2019). In our analysis, we quantify the relative ability of the two considered damping models to explain the distribution of the data in the plane of observables defined by the damping ratio and the oscillation amplitude.

In the first part of the analysis, we calculate the marginal probability of the data for each model and compute their ratio, the Bayes factor, over a two-dimensional synthetic data space. This gives a bird's eye view of the general structure of the evidence. In the second part of the analysis, Bayes factors are computed for the 101 loop oscillation events in the catalog by Nechaeva et al. (2019) with information about the oscillation amplitude.

3.1. Structure of the Evidence

Given a model M with parameter vector θ proposed to explain observed data D , a relational measure of the quality of the model derives from the integral of the joint distribution $p(\theta, D|M)$ over the full parameter space

$$\begin{aligned} p(D|M) &= \int_{\theta} p(\theta, D|M) d\theta \\ &= \int_{\theta} p(D|\theta, M) p(\theta|M) d\theta. \end{aligned} \quad (3)$$

This is the so-called marginal likelihood. In this expression, $p(\theta|M)$ is a prior distribution over the parameter space and $p(D|\theta, M)$ is the likelihood of obtaining a specific data realization as a function of the parameter vector. This measure of evidence is relational because a relation is examined to quantify how well the data D are predicted by the model M .

To apply Equation (3) to the damping models M_{NL} and M_{RA} a two-dimensional grid over synthetic data space $\mathcal{D} = (\eta, \tau_d/P)$ is constructed. The grid covers the ranges in oscillation amplitude and damping ratio in the observational and theoretical studies by Nechaeva et al. (2019) and Van Doorselaere et al. (2021). Possible data realizations over the grid are generated using the theoretical predictions given by Equations (1) and (2) for models M_{RA} and M_{NL} , respectively. Under the assumption of a Gaussian likelihood function and adopting an error model for the damping ratio alone

$$\begin{aligned} p(\mathcal{D}|\theta, M_{\text{RA,NL}}) \\ = \frac{1}{\sqrt{2\pi}\sigma} \exp \left\{ -\frac{\left[\frac{\tau_d}{P} - \frac{\tau_d(\theta)}{P} \right]_{M_{\text{RA,NL}}}^2}{2\sigma^2} \right\}, \end{aligned} \quad (4)$$

with σ the uncertainty in damping ratio. As for the priors, we choose uniform priors for the unknown parameters over

ranges similar to those in Van Doorselaere et al. (2021), additionally considering the statistical and seismological results by Aschwanden & Peter (2017); Goddard et al. (2017); Pascoe et al. (2018): $\mathcal{U}(R[\text{Mm}], 0.5, 7)$, $\mathcal{U}(\zeta, 1.1, 6)$, and $\mathcal{U}(l/R, 0.1, 2)$.

Figure 1 shows the resulting marginal likelihoods for the two damping models over the grid of synthetic data in damping ratio and oscillation amplitude. The magnitude of the marginal likelihood at each point over the surface is a measure of how well a particular combination of damping ratio and oscillation amplitude is predicted by each model. This magnitude depends on the functional form of the damping models on their parameters and is not necessarily connected with their linear/nonlinear nature. Certain damping ratio and oscillation amplitude combinations are predicted more often than others. The predictions from each model clearly differ.

For nonlinear damping (Figure 1, left panel), the significant magnitudes of marginal likelihood are distributed over the triangular region with right angle in the lower-left corner of the domain. The filled contour plot shows a convex structure with a triangular shape. The area with the highest marginal likelihood corresponds to strong damping regimes with oscillation amplitudes in the range $\sim [5, 20]$ Mm. The obtained marginal likelihood distribution offers a straightforward explanation of the spreading of samples of pairs of oscillation amplitudes and damping ratios in the Monte Carlo analysis by Van Doorselaere et al. (2021). In addition, it quantifies their relative plausibility. For linear resonant absorption (Figure 1, right panel), the region with the highest marginal likelihood corresponds to low damping ratio values, independently of the oscillation amplitude. The predictive accuracy of the model decreases for weaker damping.

The marginal likelihood values are influenced by the quality of the data, the accuracy of the models and the prior assumptions. The damping times predicted by the nonlinear model M_{NL} show certain differences with the numerical results of Magyar & Van Doorselaere (2016). The resonant damping model M_{RA} describes the long-term asymptotic state of long wavelength oscillations in tubes with thin boundaries. It overestimates the damping for thick layers (Van Doorselaere et al. 2004; Soler et al. 2014). Linear MHD simulations by Pascoe et al. (2019) show that M_{RA} significantly overestimates the damping that would occur in the first few cycles of an oscillation when l/R is not small, resulting in a model with an over-preference for low damping ratio values. This means that M_{RA} has the largest marginal likelihood precisely in the strong damping regime in which it provides the least accurate description of the oscillations, which inevitably overemphasizes the weakness of M_{RA} and hence the strength of M_{NL} . Lack of knowledge about the radial density profile (Pascoe et al. 2017b; Arregui & Goossens 2019) is an additional source of inaccuracy. Our prior sensitivity analysis showed that further increasing the upper limit for density contrast to $\zeta = 9.5$ increases the magnitude of $p(\mathcal{D}|M_{\text{NL}})$ and the marginal likelihood surface in Figure 1 (left panel) extends toward combinations with slightly larger amplitude and low damping ratio values. Because larger loop radii correspond to a lower nonlinearity parameter η/R , increasing the upper limit for R enables a greater range of τ_d/P to be consistent with a particular observed amplitude.

Overall, there is qualitative agreement between the regions with high marginal likelihood for the nonlinear damping model

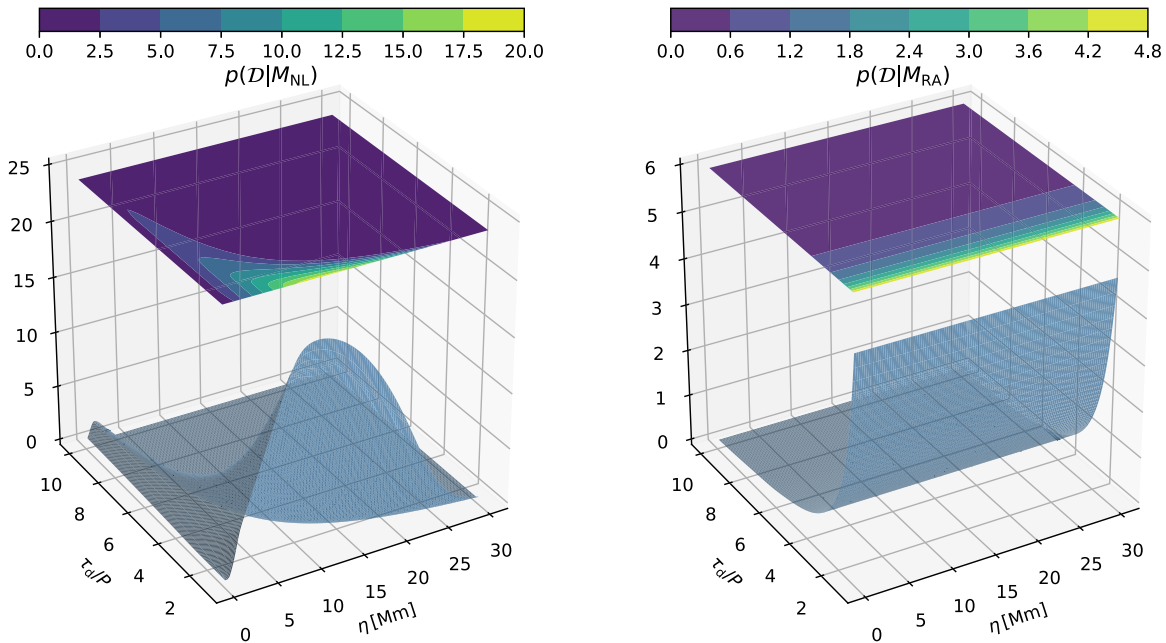


Figure 1. Surface and filled contour representations of the marginal likelihood for the damping models M_{NL} (left panel) and M_{RA} (right panel) in the synthetic data space $\mathcal{D} = (\eta, \tau_d/P)$. Equation (3) is computed over a grid with $N_\eta = 121$ and $N_{\tau_d/P} = 181$ points over the ranges $\eta \in [0.2 - 30]$ and $\tau_d/P \in [1, 10]$. The error model in the likelihood function (4) is $\sigma = 0.1\tau_d/P$.

and the broad location of observed data (compare Figure 1 (left panel) with Figure 6 in Nechaeva et al. 2019). This is suggestive of relational evidence between the observations and the nonlinear damping model.

The marginal likelihood only quantifies the evidence for a model in relation to the data that it predicts. In the general model comparison problem the aim is to assess the relative evidence between alternative models in explaining the same observed data. This is achieved with the calculation of the posterior ratio $p(M_{\text{NL}}|\mathcal{D})/p(M_{\text{RA}}|\mathcal{D})$. If the two models are equally probable a priori, $p(M_{\text{NL}}) = p(M_{\text{RA}})$ and by application of Bayes rule the posterior ratio reduces to the ratio of marginal likelihoods of the two models

$$B_{\text{NLRA}} = 2 \log \frac{p(\mathcal{D}|M_{\text{NL}})}{p(\mathcal{D}|M_{\text{RA}})} = -B_{\text{RANL}}, \quad (5)$$

where the logarithmic scale is used for convenience in the evidence assessment.

The Bayes factors B_{NLRA} and B_{RANL} defined in Equation (5) are a measure of relative evidence. They quantify the relative plausibility of each of the two models to explain the same data. To assess the levels of evidence the empirical table by Kass & Raftery (1995) is employed. For instance, the evidence in favor of model M_{NL} in front of model M_{RA} is inconclusive for values of B_{NLRA} from 0 to 2; positive for values from 2 to 6; strong for values from 6 to 10; and very strong for values above 10. A similar tabulation applies to B_{RANL} .

Figure 2 shows the resulting Bayes factor distributions over the \mathcal{D} -space. By construction, regions in this space where B_{NLRA} and B_{RANL} reach the different levels of evidence are mutually exclusive and cannot overlap. There is a clear separation between the regions where $p(\mathcal{D}|M_{\text{NL}}) > p(\mathcal{D}|M_{\text{RA}})$, thus $B_{\text{NLRA}} > 0$, from those where $p(\mathcal{D}|M_{\text{RA}}) > p(\mathcal{D}|M_{\text{NL}})$, hence $B_{\text{RANL}} > 0$.

Figure 2 (left panel) shows that the evidence supports nonlinear damping in a particular region of data space. The

region contains combinations with small oscillation amplitudes in a narrow band below ~ 5 Mm and large damping ratio and extends toward combinations with smaller damping ratio and larger oscillation amplitudes in the broader range $\sim [2, 23]$ Mm. Because $p(\mathcal{D}|M_{\text{RA}})$ is independent of oscillation amplitude, there is a conformity between the regions with high Bayes factor B_{NLRA} and marginal likelihood $p(\mathcal{D}|M_{\text{NL}})$, although their structures differ. Figure 2 (right panel) shows that the evidence supports resonant absorption in two regions. The largest one extends toward the right-hand side of the domain. Here, the large Bayes factor values in favor of resonant damping are due to the corresponding low values of $p(\mathcal{D}|M_{\text{NL}})$ relative to $p(\mathcal{D}|M_{\text{RA}})$ (see Figure 1). Because the Bayes factor represents relative strengths, one model being poor at a particular region in data space makes the alternative model seem better in comparison. The evidence in favor of resonant damping is very strong in the region restricted to combinations of very small amplitude oscillations with strong damping, close to the lower-left corner in data space.

Overall, there is qualitative agreement between the regions with high Bayes factor for the nonlinear damping model and the broad location of observed data (compare Figure 2 (left panel) with Figure 6 in Nechaeva et al. 2019). This is suggestive of evidence in favor of the nonlinear damping model relative to linear resonant absorption.

3.2. Application to Observations

The catalog by Nechaeva et al. (2019) contains information about 223 oscillating loops observed by SDO/Atmospheric Imaging Assembly (AIA) at the 171 Å extreme ultraviolet channel in the period 2010–2018 (see their Table 1). It is an extension of the catalog by Goddard et al. (2016). A subset of 101 cases contains information about both the damping ratio and the oscillation amplitude. The methods described above to compute the marginal likelihood and the Bayes factor are

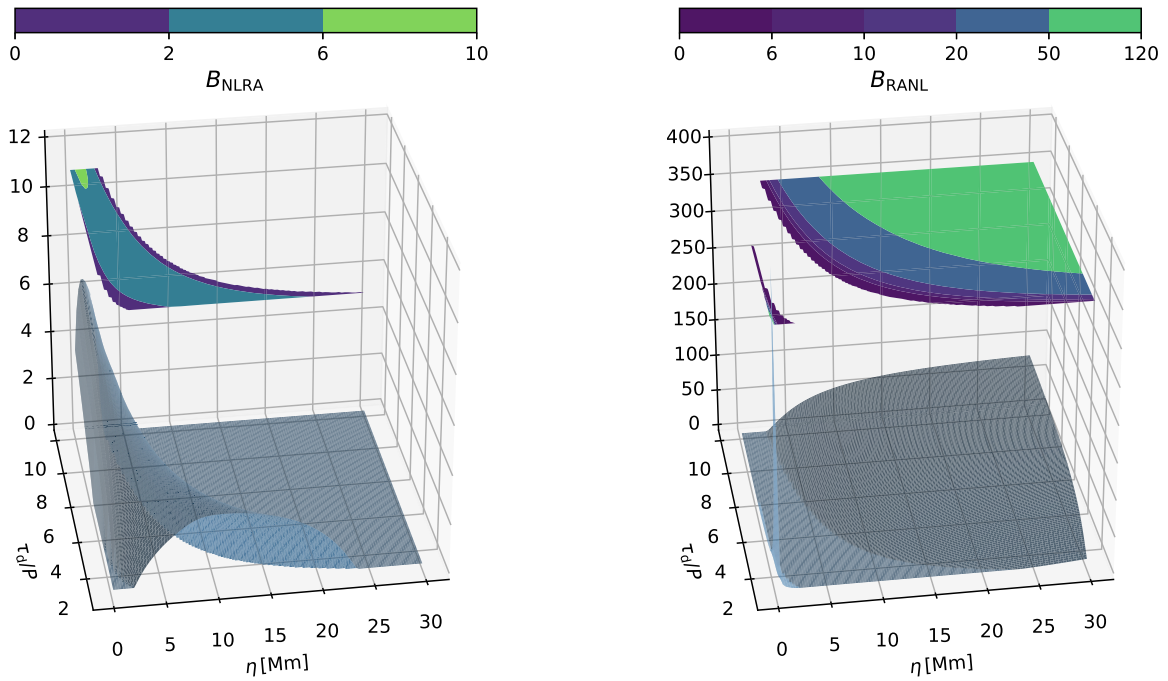


Figure 2. Surface and filled contour representations of the Bayes factors B_{NLRA} (left panel) and B_{RANL} (right panel) in the synthetic data space $\mathcal{D} = (\eta, \tau_d/P)$. Equation (5) is computed using the marginal likelihood calculations in Figure 1.

applied to them to assess the strength of the evidence for the nonlinear damping model relative to that for resonant absorption.

Table A1 in the Appendix shows a listing of the cases, with the event and loop identification numbers in Nechaeva et al. (2019); the oscillation period; the damping time; the damping ratio; and the oscillation amplitude. Instead of a grid over synthetic data space, the analysis now considers the specific pairs of measured values for oscillation amplitude and damping ratio for each event, $D = D_i = \{\eta_i, (\tau_d/P)_i\}_{i=1}^{101}$. Equations (1) and (2) with the same prior assumptions as before are used to compute the predictions from the models. Predictions are confronted to observations in the computation of the likelihood function in Equation (4) and marginal likelihoods of the models using Equation (3). The ratio of marginal likelihoods in Equation (5) gives the Bayes factor for each case. The results obtained for B_{NLRA} are given in the rightmost column of Table 1. A positive value implies evidence in favor of the nonlinear damping model. A negative value implies evidence in favor of resonant absorption. The strength of the evidence is assessed with the empirical table by Kass & Raftery (1995).

The marginal likelihood for the nonlinear damping model is larger than the marginal likelihood for resonant damping for the majority of cases, 91 out of 101 with $B_{\text{NLRA}} > 0$. The opposite happens for the remaining 10 cases with $B_{\text{NLRA}} < 0$ ($B_{\text{RANL}} > 0$). The level of evidence is conclusive in 71 cases, with Bayes factors above 2. The level of evidence is inconclusive in 30 cases, with Bayes factors below 2. The number of cases with positive evidence for the nonlinear damping model is 65 ($2 < B_{\text{NLRA}} < 6$). There is a single case with positive evidence for resonant damping ($2 < B_{\text{RANL}} < 6$). The number of cases with strong or very strong evidence for resonant damping is 5 ($B_{\text{RANL}} > 6$). The numerical values of B_{NLRA} depend on the chosen priors. Increasing the upper limit

for ζ slightly favors M_{NL} while decreasing the upper limit for R tends to favor M_{RA} .

Figure 3 shows Bayes factor, oscillation amplitude, and damping ratio values for the cases with conclusive evidence supporting either the nonlinear damping model (left panel) or resonant absorption (right panel). The 65 cases with positive evidence for the nonlinear model are grouped in the region in data space where the previous analysis of the structure of the evidence favored nonlinear damping. The six cases with positive or strong evidence for resonant damping are distributed in the complementary region where the low marginal likelihood for nonlinear damping favors resonant absorption.

Figure 4 shows the results obtained for all 101 loop oscillations, regardless of the conclusive or inconclusive nature of the evidence. The symbols and their colors indicate the corresponding levels of evidence. The pattern of evidence distribution in the general structure analysis in Section 3.1 is maintained. Among the cases with inconclusive evidence, those with larger marginal likelihood for nonlinear damping (edge-colored red circles) are located at the two sides of the main area with positive evidence for nonlinear damping. Those with larger marginal likelihood for resonant damping (edge-colored blue circles), spread further to the sides, with three of them corresponding to combinations of small amplitudes with strong damping.

The amplitudes in the observational data may be consistently underestimated, depending on the orientation of the loop and the distance of the observational slit from the loop apex, because they represent the apparent amplitude projected in the plane of the sky. Since the range of damping ratio values which can be accurately described by M_{NL} decreases for larger amplitudes (Figure 1, left panel), the effect of underestimating the actual amplitude would generally benefit this model, while having no effect on M_{RA} .

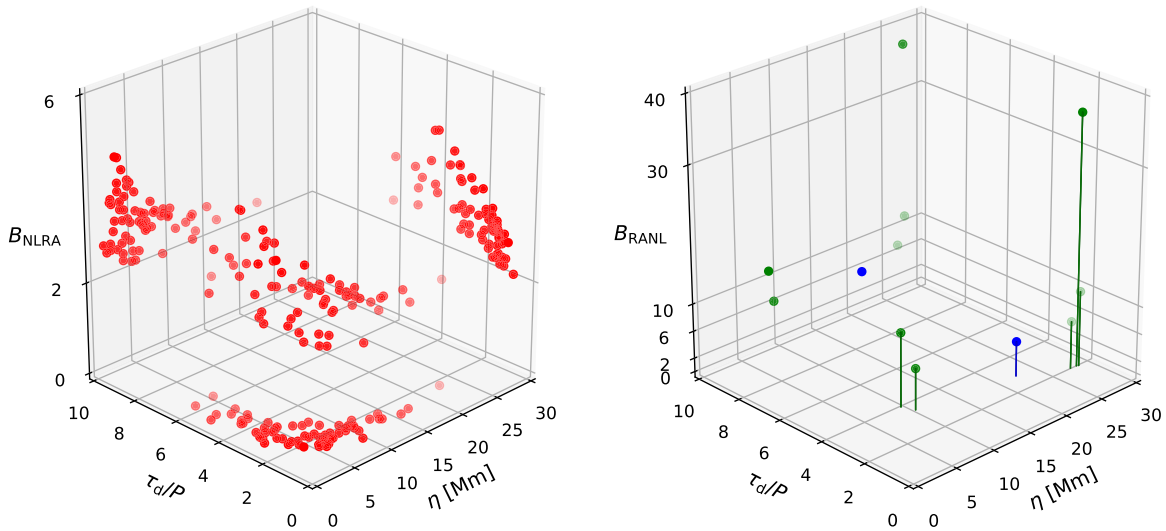


Figure 3. Bayes factor, oscillation amplitude, and damping ratio values for loop oscillations in Table 1 with positive evidence for nonlinear damping (left) and with positive (blue)/strong (green) evidence for resonant damping (right).

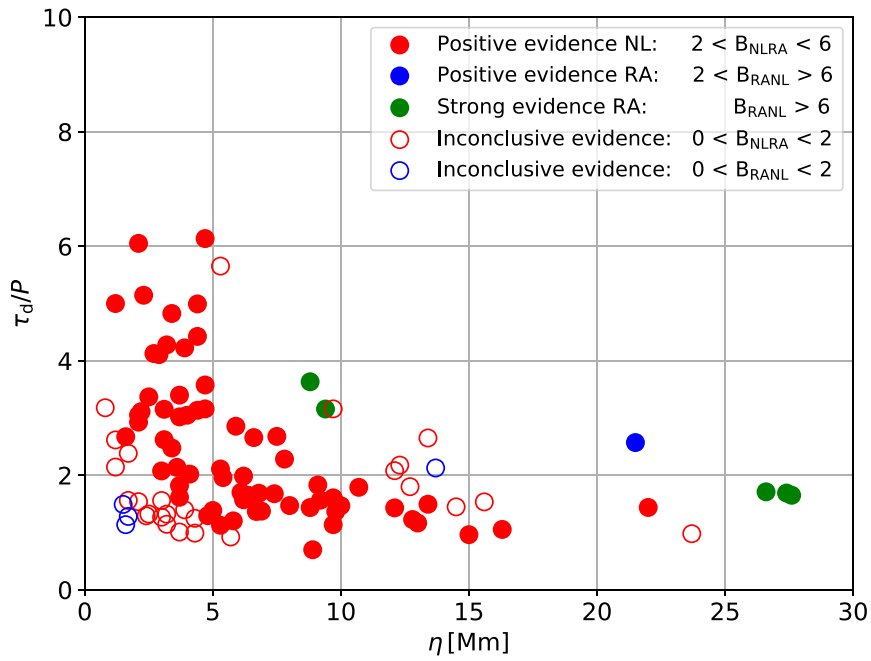


Figure 4. Scatter plot of oscillation amplitude and damping ratio values for the 101 loop oscillation cases in Table 1. Color-filled circles represent cases with conclusive evidence. Edge-colored circles represent cases with either $p(\mathcal{D}|M_{NL}) > p(\mathcal{D}|M_{RA})$ or vice versa, yet inconclusive evidence. Red is for M_{NL} , blue and green for M_{RA} .

4. Conclusion and Discussion

Our judgment about the degree of belief in a particular model to explain observed data is based on the assessment of how well the model predictions agree with observed data and on how much better this is achieved in comparison to alternative models. These relational and relative measures of the evidence for a model are given by the marginal likelihood and the Bayes factor, respectively. We considered two models postulated to explain the damping of transverse oscillations in solar coronal loops and applied those principles of Bayesian reasoning.

The structure of the evidence shows a clear separation between the regions in data space where the nonlinear damping model is more plausible relative to the linear resonant absorption model and vice versa. There is qualitative agreement

between the regions of high marginal likelihood and Bayes factor for the nonlinear damping model and the location of measured data for damping ratio and oscillation amplitude. The evidence is quantified by application to 101 loop oscillations observed with SDO/AIA. The marginal likelihood for the nonlinear damping model is larger in the majority of the cases and conclusive evidence in favor of this model is obtained in 65 cases. The cases with conclusive evidence for the nonlinear damping model outnumber those in favor of linear resonant damping by a factor of 10. The evidence for the nonlinear damping model relative to linear resonant absorption, therefore, is appreciable to a reasonable degree of Bayesian certainty.

The Bayes factor values in this study cannot be regarded in absolute terms. Their accuracy is determined by the quality of

the data, the level of refinement of the models, and the more or less informative nature of the prior assumptions. Improvement on the evidence assessment can be achieved, for example, with the use of alternative prescriptions for linear resonant absorption that more accurately describe the early stage of loop oscillations, as appropriate for the observational cases of strong damping (Hood et al. 2013; Pascoe et al. 2019), the consideration of additional physical effects (Pascoe et al. 2017b), or by further constraining the prior densities through seismological inference of the unknown parameters (Nisticò et al. 2013; Pascoe et al. 2016, 2017a).

The availability of specific model parameters also affects the calculated Bayes factors. As an example, consider entry number $i=26$ in Table 1, with $B_{\text{NLRA}} = -10.9$. For this event, first studied by Nisticò et al. (2013), estimates for loop radius, $R \sim 3.3$ Mm; density contrast, $\zeta \sim 3$; and thickness of the layer, $l/R \sim 0.5$, are available (Pascoe et al. 2016, 2017a, 2017b). In contrast to the value of $\eta = 8.8$ Mm for the amplitude reported in the catalog, Pascoe et al. (2017b) quote a value of $\eta \sim 2$ Mm. Bayes factor calculations, now without the need to perform integration over parameter space, lead to values of $B_{\text{NLRA}} \sim 13$ for

$\eta = 2.2$ Mm and $B_{\text{NLRA}} \sim -75$ for $\eta = 8.8$ Mm, which give support to the nonlinear model and also point to an overestimation of the amplitude in the catalog.

In general, because of our inability to directly measure the relevant physical parameters, the Bayesian approach offers the best course of action for judgment under uncertainty and offers principled ways to improve the evidence assessment as better data, more refined models and more informative priors become available.

This research was supported by project PGC2018-102108-B-I00 from Ministerio de Ciencia, Innovación y Universidades and FEDER funds.

Facility: SDO/AIA (Lemen et al. 2012).

Software: NumPy (Harris et al. 2020), Matplotlib (Hunter 2007).

Appendix

Table A1 presents the results of the analysis described in Section 3.2.

Table A1
Loop Oscillation Data from Nechaeva et al. (2019) and Computed Bayes Factors

i	Event ID	Loop ID	P [minutes]	τ_D [minutes]	τ_D/P	η [Mm]	B_{NLRA}
1	1	1	3.42 ± 0.06	5.34 ± 1.12	1.56 ± 0.33	1.7	0.7
2	1	2	4.11 ± 0.05	10.76 ± 2.79	2.62 ± 0.68	1.2	1.5
3	3	1	2.46 ± 0.03	8.8 ± 1.8	3.58 ± 0.73	4.7	3.9
4	3	2	3.62 ± 0.08	4.12 ± 0.47	1.14 ± 0.13	9.7	2.8
5	4	1	2.29 ± 0.03	7.18 ± 1.5	3.14 ± 0.66	4.4	3.9
6	4	2	3.47 ± 0.03	7.44 ± 1.	2.14 ± 0.29	1.2	1.2
7	7	1	1.69 ± 0.02	7.23 ± 1.3	4.28 ± 0.77	3.2	4.5
8	8	1	3.74 ± 0.07	10. ± 1.	2.67 ± 0.27	1.6	2.5
9	9	1	5.14 ± 0.17	5.09 ± 0.98	0.99 ± 0.19	4.3	1.3
10	9	2	8.95 ± 0.14	11.83 ± 4.76	1.32 ± 0.53	3.2	1.4
11	10	1	11.46 ± 0.17	8.02 ± 1.09	0.70 ± 0.10	8.9	2.0
12	11	3	2.6 ± 0.05	8.84 ± 1.5	3.40 ± 0.58	3.7	4.2
13	14	2	2.35 ± 0.07	2.69 ± 0.64	1.14 ± 0.27	3.2	1.0
14	15	1	2.07 ± 0.04	9.99 ± 4.59	4.83 ± 2.22	3.4	3.4
15	16	2	9.52 ± 0.11	12.2 ± 3.47	1.28 ± 0.36	1.7	-0.1
16	17	2	11.27 ± 0.12	16.55 ± 1.44	1.47 ± 0.13	10.0	3.0
17	18	1	5.36 ± 0.23	16.19 ± 7.67	3.02 ± 1.44	3.7	3.1
18	21	1	15.36 ± 0.4	19.19 ± 1.55	1.25 ± 0.11	4.3	2.0
19	22	1	17.86 ± 0.3	27.43 ± 4.26	1.54 ± 0.24	15.6	0.7
20	22	3	20.46 ± 0.58	35.01 ± 6.44	1.71 ± 0.32	26.6	-7.0
21	23	1	5.13 ± 0.11	8. ± 5.	1.56 ± 0.98	3.0	1.8
22	24	1	11.95 ± 0.13	18.71 ± 4.5	1.57 ± 0.38	9.2	2.9
23	26	1	3.71 ± 0.05	7.83 ± 0.62	2.11 ± 0.17	5.3	3.6
24	27	1	7.67 ± 0.04	24.22 ± 2.02	3.16 ± 0.26	9.4	-6.2
25	27	2	9.59 ± 0.09	17.57 ± 2.35	1.83 ± 0.25	9.1	3.0
26	28	1	4.28 ± 0.02	15.55 ± 1.22	3.63 ± 0.29	8.8	-10.9
27	28	2	3.38 ± 0.02	19.11 ± 4.85	5.65 ± 1.44	5.3	1.7
28	30	1	9.95 ± 0.27	16.7 ± 1.03	1.68 ± 0.11	7.4	3.3
29	34	2	5.2 ± 0.08	15.23 ± 5.5	2.93 ± 1.06	2.1	2.7
30	36	2	5.61 ± 0.03	24.83 ± 3.41	4.43 ± 0.61	4.4	3.8
31	36	4	5.53 ± 0.04	7.32 ± 1.08	1.32 ± 0.20	2.5	1.0
32	36	7	5.72 ± 0.06	14.17 ± 2.73	2.48 ± 0.48	3.4	3.5
33	36	8	4.33 ± 0.08	9.01 ± 2.16	2.08 ± 0.50	12.1	1.3
34	36	9	6.18 ± 0.05	13.15 ± 2.66	2.13 ± 0.43	13.7	-0.4
35	37	1	7.14 ± 0.07	7.53 ± 1.45	1.05 ± 0.20	16.3	2.3
36	37	2	3.6 ± 0.03	9.44 ± 0.92	2.62 ± 0.26	3.1	3.8
37	37	3	8.35 ± 0.08	15.04 ± 1.81	1.80 ± 0.22	12.7	1.2
38	37	5	4.5 ± 0.02	14. ± 2.	3.11 ± 0.44	2.2	3.7
39	38	1	7.23 ± 0.06	15.75 ± 3.09	2.18 ± 0.43	12.3	0.4
40	38	2	9.78 ± 0.19	14.62 ± 4.96	1.49 ± 0.51	13.4	2.3

Table A1
(Continued)

i	Event ID	Loop ID	P [minutes]	τ_D [minutes]	τ_D/P	η [Mm]	B_{NLRA}
41	38	3	6.95 ± 0.14	$9. \pm 3.$	1.29 ± 0.43	4.8	2.1
42	39	1	2.48 ± 0.04	7.82 ± 1.66	3.15 ± 0.67	3.1	4.0
43	42	1	15.28 ± 0.16	21.98 ± 15.6	1.44 ± 1.02	22.0	2.3
44	42	2	15.76 ± 0.12	26.64 ± 2.17	1.69 ± 0.14	27.4	-36.8
45	42	3	16.08 ± 0.21	15.76 ± 3.09	0.98 ± 0.19	23.7	0.8
46	43	4	10.45 ± 0.17	15.38 ± 2.58	1.47 ± 0.25	8.0	3.1
47	43	5	8.03 ± 0.18	9.37 ± 1.22	1.17 ± 0.15	13.0	2.7
48	46	5	4.8 ± 0.1	19.72 ± 3.23	4.11 ± 0.68	2.9	4.5
49	48	1	9.07 ± 0.14	20.71 ± 4.71	2.28 ± 0.52	7.8	3.0
50	48	2	11.88 ± 0.13	19.62 ± 2.96	1.65 ± 0.25	27.6	-11.1
51	48	5	13.5 ± 0.16	24.17 ± 5.13	1.79 ± 0.38	10.7	2.5
52	48	7	14.16 ± 0.55	13.64 ± 3.93	0.96 ± 0.28	15.0	2.7
53	49	1	8.52 ± 1.02	8.6 ± 3.6	1.01 ± 0.44	3.7 ± 1.7	1.2
54	50	1	7.36 ± 0.26	24.8 ± 12.1	3.37 ± 1.65	2.5 ± 0.6	3.0
55	51	2	13.75 ± 0.38	23.2 ± 8.9	1.69 ± 0.65	6.8 ± 1.5	2.9
56	52	1	13.51 ± 0.42	27.3 ± 11.1	2.02 ± 0.82	4.1 ± 0.8	2.7
57	52	2	12.95 ± 0.73	15.6 ± 4.4	1.20 ± 0.35	5.8 ± 1.5	2.3
58	53	1	16.17 ± 0.42	43.0 ± 13.5	2.66 ± 0.84	6.6 ± 1.3	3.1
59	54	1	11.16 ± 0.86	18.4 ± 8.2	1.65 ± 0.75	6.4 ± 1.6	2.8
60	56	3	11.83 ± 0.38	31.7 ± 10.6	2.68 ± 0.90	7.5 ± 1.3	2.7
61	57	2	2.89 ± 0.09	6.0 ± 1.8	2.08 ± 0.63	3.0 ± 0.8	2.5
62	58	1	3.44 ± 0.46	8.2 ± 4.6	2.38 ± 1.37	1.7 ± 1.0	1.5
63	59	1	5.19 ± 0.33	11.1 ± 5.2	2.14 ± 1.01	3.6 ± 1.2	2.6
64	60	3	9.59 ± 0.66	27.4 ± 12.5	2.86 ± 1.32	5.9 ± 2.2	2.9
65	63	1	4.45 ± 0.07	27.3 ± 10.2	6.13 ± 2.29	4.7 ± 0.9	2.6
66	64	1	2.17 ± 0.13	6.9 ± 3.6	3.18 ± 1.67	0.8 ± 0.3	0.5
67	64	3	7.19 ± 0.20	35.9 ± 14.1	4.99 ± 1.97	4.4 ± 0.5	3.1
68	64	5	20.76 ± 1.03	28.4 ± 7.3	1.37 ± 0.36	9.8 ± 2.4	2.8
69	64	6	20.43 ± 0.47	29.6 ± 7.5	1.45 ± 0.37	14.5 ± 2.6	1.9
70	65	2	17.82 ± 0.49	25.6 ± 6.9	1.44 ± 0.39	8.8 ± 2.0	2.9
71	66	1	2.38 ± 0.05	14.4 ± 7.0	6.05 ± 2.94	2.1 ± 0.4	3.6
72	67	1	17.19 ± 0.76	21.1 ± 5.8	1.23 ± 0.34	12.8 ± 3.6	2.6
73	68	1	7.34 ± 0.66	11.3 ± 5.0	1.54 ± 0.70	2.1 ± 0.8	0.9
74	69	1	6.22 ± 0.18	32.0 ± 14.8	5.14 ± 2.38	2.3 ± 0.5	3.5
75	69	2	12.81 ± 0.32	21.8 ± 4.6	1.70 ± 0.36	6.1 ± 1.3	3.1
76	70	2	9.85 ± 0.40	15.5 ± 4.3	1.57 ± 0.44	6.2 ± 1.7	2.9
77	70	3	5.56 ± 0.16	27.8 ± 13.7	5.00 ± 2.47	1.2 ± 0.3	2.7
78	72	1	13.30 ± 0.72	18.2 ± 5.9	1.37 ± 0.45	6.7 ± 1.8	2.7
79	72	2	6.82 ± 0.15	20.8 ± 6.4	3.05 ± 0.94	4.0 ± 0.7	3.6
80	72	4	18.59 ± 0.78	49.3 ± 20.6	2.65 ± 1.11	13.4 ± 2.1	1.4
81	73	1	10.21 ± 0.48	16.5 ± 4.6	1.62 ± 0.46	3.7 ± 0.9	2.2
82	74	2	4.85 ± 0.23	14.8 ± 6.8	3.05 ± 1.41	2.1 ± 0.6	2.6
83	74	3	2.90 ± 0.27	3.3 ± 1.0	1.14 ± 0.36	1.6 ± 0.7	-0.7
84	75	1	10.76 ± 0.28	15.4 ± 3.8	1.43 ± 0.36	12.1 ± 1.1	2.5
85	75	2	8.48 ± 0.16	26.8 ± 7.6	3.16 ± 0.90	9.7 ± 1.2	1.0
86	75	3	8.71 ± 0.42	17.3 ± 5.4	1.99 ± 0.63	6.2 ± 1.5	3.1
87	77	1	7.69 ± 0.50	24.3 ± 12.8	3.16 ± 1.68	4.7 ± 1.4	3.0
88	78	2	5.88 ± 0.43	7.6 ± 2.7	1.29 ± 0.47	2.4 ± 1.1	0.7
89	79	3	2.95 ± 0.33	4.4 ± 2.2	1.49 ± 0.76	1.5 ± 0.8	-0.0
90	80	1	12.51 ± 0.57	20.1 ± 5.5	1.61 ± 0.45	9.7 ± 2.5	2.8
91	80	2	9.69 ± 0.26	19.0 ± 4.8	1.96 ± 0.50	5.4 ± 1.4	3.2
92	81	1	11.35 ± 0.83	14.4 ± 5.1	1.27 ± 0.46	3.0 ± 1.1	1.2
93	83	1	5.99 ± 0.51	10.9 ± 4.6	1.82 ± 0.78	3.7 ± 1.2	2.4
94	84	1	3.78 ± 0.33	15.6 ± 8.3	4.13 ± 2.23	2.7 ± 1.0	3.2
95	87	1	5.94 ± 0.32	25.1 ± 10.8	4.23 ± 1.83	3.9 ± 1.0	3.3
96	87	2	9.24 ± 0.62	12.7 ± 4.6	1.37 ± 0.51	6.9 ± 2.2	2.7
97	88	1	9.38 ± 0.19	13.0 ± 5.4	1.39 ± 0.58	5.0 ± 0.4	2.4
98	88	3	13.75 ± 1.18	15.5 ± 6.5	1.13 ± 0.48	5.3 ± 1.8	2.1
99	90	1	9.32 ± 0.31	8.6 ± 2.4	0.92 ± 0.26	5.7 ± 1.4	1.8
100	92	1	6.51 ± 0.31	9.1 ± 2.4	1.40 ± 0.37	3.9 ± 1.3	2.0
101	93	1	8.32 ± 0.10	21.4 ± 4.9	2.57 ± 0.59	21.5 ± 2.4	-5.2

Note. The table gives the entry number i , event ID, loop ID, oscillation period P , damping time τ_D , damping rate τ_D/P , oscillation amplitude η , and computed Bayes factor $B_{\text{NLRA}} = -B_{\text{RANL}}$. Errors for damping ratio are calculated from those for period and damping time as $R_{\tau_D/P} = \sqrt{R_{\tau_D}^2 + R_P^2}$, where R refers to the relative error.

ORCID iDs

Iñigo Arregui  <https://orcid.org/0000-0002-7008-7661>

References

- Arregui, I. 2018, *AdSpR*, **61**, 655
- Arregui, I., & Goossens, M. 2019, *A&A*, **622**, A44
- Aschwanden, M. J., Fletcher, L., Schrijver, C. J., & Alexander, D. 1999, *ApJ*, **520**, 880
- Aschwanden, M. J., & Peter, H. 2017, *ApJ*, **840**, 4
- Goddard, C. R., & Nakariakov, V. M. 2016, *A&A*, **590**, L5
- Goddard, C. R., Nisticò, G., Nakariakov, V. M., & Zimovets, I. V. 2016, *A&A*, **585**, A137
- Goddard, C. R., Pascoe, D. J., Anfinogentov, S., & Nakariakov, V. M. 2017, *A&A*, **605**, A65
- Goossens, M., Andries, J., & Arregui, I. 2006, *RSPTA*, **364**, 433
- Goossens, M., Andries, J., & Aschwanden, M. J. 2002, *A&A*, **394**, L39
- Goossens, M., Erdélyi, R., & Ruderman, M. S. 2011, *SSRv*, **158**, 289
- Gregory, P. C. 2005, *Bayesian Logical Data Analysis for the Physical Sciences: A Comparative Approach with ‘Mathematica’ Support* (Cambridge: Cambridge Univ. Press)
- Harris, C. R., Millman, K. J., van der Walt, S. J., et al. 2020, *Natur*, **585**, 357
- Hood, A. W., Ruderman, M., Pascoe, D. J., et al. 2013, *A&A*, **551**, A39
- Hunter, J. D. 2007, *CSE*, **9**, 90
- Jaynes, E. T. 2003, *Probability Theory: The Logic of Science* (Cambridge: Cambridge Univ. Press)
- Kass, R. E., & Raftery, A. E. 1995, *JASA*, **90**, 773
- Lemen, J. R., Title, A. M., Akin, D. J., et al. 2012, *SoPh*, **275**, 17
- Lindley, D. V. 2014, *Understanding Uncertainty* (New York: Wiley)
- Magyar, N., & Van Doorselaere, T. 2016, *A&A*, **595**, A81
- Nakariakov, V. M., Ofman, L., DeLuca, E. E., Roberts, B., & Davila, J. M. 1999, *Sci*, **285**, 862
- Nechaeva, A., Zimovets, I. V., Nakariakov, V. M., & Goddard, C. R. 2019, *ApJS*, **241**, 31
- Nisticò, G., Nakariakov, V. M., & Verwichte, E. 2013, *A&A*, **552**, A57
- Pascoe, D. J., Anfinogentov, S., Nisticò, G., Goddard, C. R., & Nakariakov, V. M. 2017a, *A&A*, **600**, A78
- Pascoe, D. J., Anfinogentov, S. A., Goddard, C. R., & Nakariakov, V. M. 2018, *ApJ*, **860**, 31
- Pascoe, D. J., Goddard, C. R., Anfinogentov, S., & Nakariakov, V. M. 2017b, *A&A*, **600**, L7
- Pascoe, D. J., Goddard, C. R., Nisticò, G., Anfinogentov, S., & Nakariakov, V. M. 2016, *A&A*, **589**, A136
- Pascoe, D. J., Hood, A. W., & Van Doorselaere, T. 2019, *FrASS*, **6**, 22
- Ruderman, M. S., & Roberts, B. 2002, *ApJ*, **577**, 475
- Soler, R., Goossens, M., Terradas, J., & Oliver, R. 2014, *ApJ*, **781**, 111
- Van Doorselaere, T., Andries, J., Poedts, S., & Goossens, M. 2004, *ApJ*, **606**, 1223
- Van Doorselaere, T., Goossens, M., Aagyar, N., Ruderman, M. S., & Ismayilli, R. 2021, *ApJ*, **910**, 58